High-accuracy measurement of mass attenuation coefficients and the imaginary component of the atomic form factor of zinc from 8.51 keV to 11.59 keV, and X-ray absorption fine structure with investigation of zinc theory and nanostructure

Ruwini S. K. Ekanayake,[a] Christopher T. Chantler,[a]* Daniel Sier,[a] Martin J. Schalken,[a] Alexis J. Illig,[a] Martin D. de Jonge,[b] Bernt Johannessen,[b] Peter Kappen[b] and Chanh Q. Tran[c]

[a]School of Physics, University of Melbourne, Australia, [b]ANSTO, Australian Synchrotron, Melbourne, Australia, and [c]La Trobe University, Australia. *Correspondence e-mail: chantler@unimelb.edu.au

High-accuracy X-ray mass attenuation coefficients were measured from the first X-ray Extended Range Technique (XERT)-like experiment at the Australian Synchrotron. Experimentally measured mass attenuation coefficients deviate by ~50% from the theoretical values near the zinc absorption edge, suggesting that improvements in theoretical tabulations of mass attenuation coefficients are required to bring them into better agreement with experiment. Using these values the imaginary component of the atomic form factor of zinc was determined for all the measured photon energies. The zinc K-edge jump ratio and jump factor are determined and results raise significant questions regarding the definitions of quantities used and best practice for background subtraction prior to X-ray absorption fine-structure (XAFS) analysis. The XAFS analysis shows excellent agreement between the measured and tabulated values and yields bond lengths and nanostructure of zinc with uncertainties of from 0.1% to 0.3% or 0.003 Å to 0.008 Å. Significant variation from the reported crystal structure was observed, suggesting local dynamic motion of the standard crystal lattice. XAFS is sensitive to dynamic correlated motion and *in principle* is capable of observing local dynamic motion beyond the reach of conventional crystallography. These results for the zinc absorption coefficient, XAFS and structure are the most accurate structural refinements of zinc at room temperature.

1. Introduction

X-ray attenuation coefficients and atomic form factors explain how X-rays interact with matter and atoms (Rontgen, 1896). X-ray absorption fine-structure (XAFS) spectra display the energy-dependent fine structure in the mass attenuation coefficients, sensitive to many structural details of materials (Rehr & Albers, 2000). Thus, X-ray mass attenuation coefficients, particularly across absorption edge regions, are widely used in many techniques and fields including biological (Coulthard & Sham, 1996; Streltsov et al., 2018), molecular, condensed matter and solid state fields (Palmberg & Rhodin, 1968; Bohic et al., 2001) to study structural parameters including bond lengths, thermal parameters, oxidation number, coordination number and electron inelastic mean free paths of materials and molecules (Ignatov et al., 2001; Han et al., 2002; Islam et al., 2015, 2016). Attenuation coefficients and atomic form factors are important in the study of the

HCP
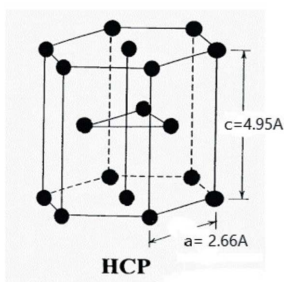
density of electron states (Joly *et al.*, 1999; Hossain *et al.*, 2005), roughness of sample surfaces (Glover *et al.*, 2009), dynamics of atomic processes, elastic scattering and other scattering of X-ray interactions with matter (Hopersky *et al.*, 2004) and self-absorption of materials (Trevorah *et al.*, 2019). Mass attenuation across the XAFS can be used to confirm or determine near-neighbour coordination lengths of materials (Sayers *et al.*, 1972; Glover *et al.*, 2010).

Many improvements and developments in analytic techniques and experiment have been introduced in XAFS analysis including the XERT protocol for high-accuracy data with uncertainties below 0.1% and removal of systematic errors (Chantler, 2009). The XAFS spectrum consists of oscillations at energies just after the absorption edge due to the interference of the photoelectron wave with the neighbouring electrons (Joly, 2001). The oscillations can be investigated using *FEFF* (Rehr *et al.*, 1991; Rehr & Albers, 2000) and *eFEFFIT* (Smale *et al.*, 2006; Schalken & Chantler, 2018), from modified *IFEFFIT* (Newville, 2001) analysis propagating robust uncertainties of XAFS data over the entire energy spectrum. The implementation of the XERT-like experiment, the first in Australia, is presented by Ekanayake *et al.* (2021), hereafter called Part 1.

This paper presents X-ray mass attenuation coefficients and derivations of the imaginary component of the atomic form factor of zinc to a high accuracy. Experimental details and systematic corrections are provided in Part 1. The photoelectric mass absorption coefficient is also calculated from the mass attenuation coefficient after subtracting the scattering contribution. These measurements can be used as standards in XAFS and are also useful in crystallography and medical fields. These high-accuracy data permit direct access to critical measurements of electron inelastic mean free paths (IMFPs) and other key parameters. Discrepancies between the tabulated and the high-accuracy experimental values are investigated. X-ray mass attenuation coefficients are calculated using relativistic quantum mechanics under several assumptions. *XCOM* (Berger & Hubbell, 1987) and *FFAST* (Chantler, 1995, 2000) are the two theoretical tabulations recommended by the National Institute of Standards and Technology (NIST). *XCOM* tabulated unrenormalized values with Hartree–Slater non-relativistic wavefunctions (Berger & Hubbell, 1987) and renormalized values with relativistic Hartree–Fock potential (Scofield, 1973) are compared with experiment. The use of renormalization has been an ongoing discussion in the field.

The edge jump ratio r is the ratio of the mass photoabsorption coefficient just above the absorption edge to the mass photoabsorption coefficient just below the absorption edge (McMaster *et al.*, 1969; Veigele, 1973; Broll, 1986; Bennal & Badiger, 2007; Kaya *et al.*, 2011). Investigation of the experimental edge jump J, or J_K for the K-edge, and the edge jump ratio r, or r_K here, is important for better understanding of absorption spectra since it checks the predictions of theory which are often used from tabulations for many applications. The edge jump is generally important for radiology, shielding, X-ray filters, reference materials, X-ray fluorescence (Budak *et*

al., 2003) and in particular applications for individual elements or materials including, for example, characterization of dopants in superconductors (Mallikarjuna *et al.*, 2002). In many cases oxides or other compounds have been used which complicated any analysis. The zinc K-edge jump ratio and jump factor raise significant questions about how to define the edge and the background subtraction prior to XAFS analysis.

XAFS analysis was performed on the above calculated measurements and the bond lengths of zinc were determined. These high-accuracy values can be used as a baseline to discriminate different IMFP theories for zinc data.

2. The mass attenuation coefficients and imaginary component of the atomic form factor

The mass attenuation coefficients were obtained by considering the mean of the results from measurements using different foils and apertures. Evaluated values of mass attenuation coefficients with the uncertainties along the interested energy region are plotted in Fig. 1.

The imaginary component of the form factor can be derived from the photoelectric mass absorption coefficients $[\mu/\rho]_{pe}$,

$$f_2 = \frac{EuA[\mu/\rho]_{pe}}{2hcR_e}, \qquad (1)$$

where E is the energy, u is the atomic mass unit, A is the atomic mass, R_e is the classic electron radius, h is the plank constant and c is the speed of light. The photoelectric absorption is the dominant contribution for the total mass attenuation and it can be derived by subtracting the attenuation contributions due to Coherent (Rayleigh) and incoherent (Compton) scatterings. These scattering contributions $[\mu/\rho]_{R+C}$ were obtained from the *FFAST* calculations.

Additional uncertainties were estimated to be the half of the discrepancy between the *XCOM* and *FFAST* tabulated $[\mu/\rho]_{R+C}$ values. The scattering uncertainties are always less than 0.036% of the photoelectric absorption coefficient. The uncertainty of f_2 is

$$\sigma_{f_2} = \frac{EuA}{2hcR_e} \left(\sigma_{[\mu/\rho]}^2 + \Delta_{R+C}^2 \right)^{1/2}. \qquad (2)$$

This work demonstrates the attenuation measurements of zinc over an extended energy range including K-edge XAFS spectrum from XERT and solid-state properties of the sample on an absolute scale. The energy-dependent mass attenuation coefficients from 34.77 to 327.76 (cm^2 g^{-1}) were calculated over the energy range from 8.51 keV to 11.5914 keV. The absolute experimental uncertainties range from 0.023% to 0.036%, limited by various experimental systematic errors such as energy drifts during the monochromator tuning, monochromator glitches, and ion chamber current fluctuations.

Quantifying uncertainties is crucial in identifying any data affected by any systematics. Often badly affected points are deleted by researchers; yet a quantitative uncertainty including variance can validate them with an appropriate weighting from the inconsistency. The imaginary component
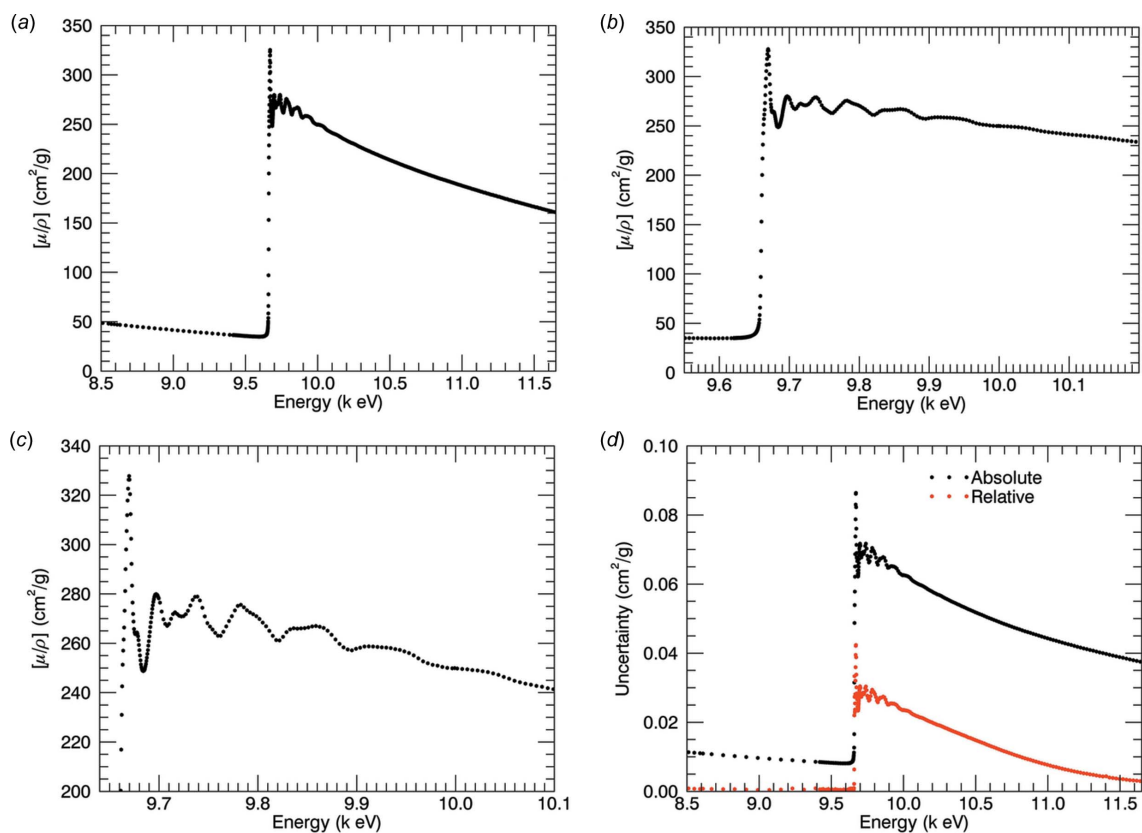
Figure 1
Calculated mass attenuation coefficient of zinc (*a*) over the energy range 8.51 keV to 11.59 keV; (*b*) covering the edge and XAFS region; (*c*) in the central XAFS region; and (*d*) absolute and relative percentage uncertainties. The zinc *K*-absorption edge is observed at 9.66 keV and the associated XAFS lies between 9.66 keV and 10.10 keV.

of the atomic form factor was determined to be from 0.492 (e atom^{-1}) to 4.898 (e atom^{-1}). Uncertainty contributions and the dominant systematic corrections in the current work are summarized in Table 1. Table S1 of the supporting information provides: the measured mass attenuation coefficients $[\mu/\rho]_{pe}$ or $[\mu/\rho]_{tot}$ as a function of energy with energy E and estimated energy uncertainty σ_E; the total (or absolute) estimated percentage uncertainties $\sigma_{[\mu/\rho]_{tot}}\%$ and estimated relative percentage uncertainties $\sigma_{[\mu/\rho]_{rel}}\%$; the mass photoabsorption coefficient $[\mu/\rho]_{pe}$ (cm^2 g^{-1}) with percentage uncertainties $\sigma_{[\mu/\rho]_{pe}}\%$, particularly after subtraction of the estimated scattering coefficients (Rayleigh and Compton), are provided in later columns, together with the estimated imaginary component of the atomic form factor f_2 (e atom^{-1}).

Supplementary documents are provided including the data of Table S1 in text format (see ZnTable2.dat in the supporting zip file). The format of $[\mu/\rho]_{tot}$ (cm^2 g^{-1}) versus E with uncertainties (Zn_K_muoverrhovsE.dat) provides input for *efeffit* (Smale *et al.*, 2006; Schalken & Chantler, 2018), *IFEFFIT* (Newville, 2001), *Athena* (Ravel & Newville, 2005) and particularly *mu2chi* (Schalken & Chantler, 2018). Corresponding files are represented as a template for both a cif standard (Zn_K.cif) and χ versus k with uncertainties (Zn_K_eFEFFIT.dat) data for an *efeffit*, *IFEFFIT* and *Athena* input standard.
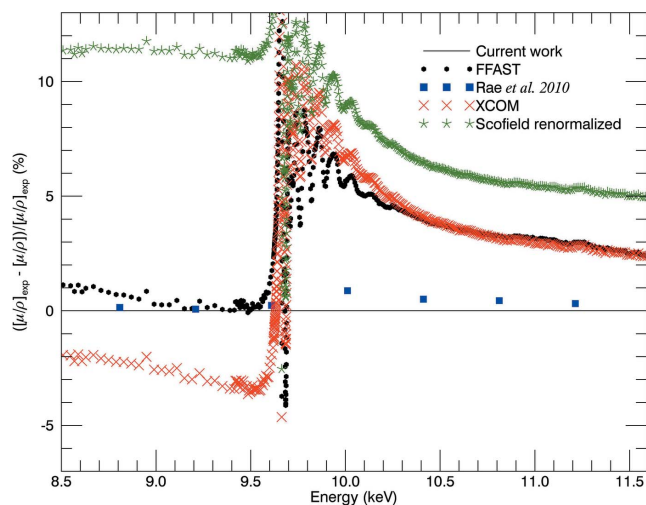

Figure 2
The percentage discrepancy between the derived mass attenuation coefficient and the tabulated *FFAST* values (circles) (Chantler, 2000) over the energy range 8.5 keV to 11.59 keV, and the percentage discrepancies between *XCOM* tabulated values with Hartree–Slater calculations (crosses) (Berger & Hubbell, 1987), Scofield tabulated values renormalized with Hartree–Fock calculations (stars) (Scofield, 1973) and Rae *et al.* (2010) measurements (squares). The near-edge region has a large discrepancy from current measurements due to the solid-state XAFS structure and the triangle effect. Renormalized Scofield (1973) values deviate dramatically everywhere, implying that the earlier belief that correct theory lies between the unrenormalized and the renormalized predictions is not valid for these data.

Table 1
Uncertainty and variation of mass attenuation coefficients during processing at several systematic correction stages; and the magnitude of specific systematic corrections.

Contributions to measurements are labelled $[\mu/\rho]_{rel}$ if they particularly contribute to the relative structure of adjacent points, the edge shape or the XAFS; or $[\mu/\rho]_{abs}$ if they primarily scale all values with a slowly varying function. Hence there are two final uncertainties – relating to the absolute value of the mass attenuation coefficient $[\mu/\rho]$ and relating to the point-wise and local structure, for example, for XAFS analysis which can be denoted $[\mu/\rho]_{rel}$.

Quantity	Magnitude of correction $[\mu/\rho]$	Uncertainty and variance $\sigma_{[\mu/\rho]}$	Comments
$[\mu/\rho]_{rel}$		<0.319%	Variance[a]
	22–536% (10 μm foil)	<1.853% (10 μm)	Blank normalization[b]
	Up to 97% (50 μm foil)	<0.133% (100 μm)	
	Up to 57% ±15% (100 μm)	0.00039–1.46%	Dark current[c]
	Up to 1.31% (10 μm)		
(total)		<0.042%	Total variance after corrections[d]
	1–5×10^{-3}%		Harmonic correction[e]
(50 μm)	<14.2%	<10.5%	Fluorescence correction[f]
(25 μm)	<0.101%	<0.003%	
(10 μm)	<0.0123%	<0.0003%	
(total)	<0.139%	<0.028%	
(10 μm)	<2.52%	<0.02%	Roughness[g]
(25 μm)	<0.815%	<0.015%	
(total)	<1.56%	<0.0037%	
(50 μm)	<9.89%	<0.239%	Bandwidth[h]
(25 μm)	<4.91%	<0.119%	
(10 μm)	<1.703%	<0.041%	
(total)	<7.24%	<0.0037%	
$[\mu/\rho]_{abs}$		<0.037%	Nominal thicknesses[i]
	3.55–7.60%	0.000018–0.024237%	Average ICD[j]
	0.374–7.606%	<0.024%	Full-foil map[k]
E (keV)	−1 to +3 eV, ±1–3 eV	<0.0038%	Energy[l]

Quantity	Magnitude range (cm² g⁻¹)	Uncertainty range $\sigma_{[\mu/\rho]}$	Comments
$[\mu/\rho]_{rel}$	34.765–325.321	0.000677–0.027%	After systematic corrections[m]
$[\mu/\rho]_{abs}$	34.765–327.760	0.023–0.0357%	After normalizing to absolute thickness from full-foil map[n]

[a] Standard errors from counting statistics (variance including precision before systematic corrections). [b] Blank correction and net uncertainty (Part 1, §3). Large for thin foils. [c] Dark current correction and net uncertainty (±0.5 counts s⁻¹) (Part 1, §3). [d] Total dispersion of measurement precision after above corrections. [e] Harmonic coefficient and contribution is very small here (Part 1, §7). [f] Secondary photons from fluorescent scattering. Correction large for 50 μm sample and directly above absorption edges, 0 below Zn edge (Part 1, §6). Maximum uncertainty only applies to 50 μm. [g] Effect of roughness is greatest for 10 μm sample when attenuation is large (Part 1, §8). [h] Bandwidth correction greatest for 50 μm sample along the edge where d[μ/ρ]/dE is greatest. [i] Use of nominal thickness and corresponding uncertainty (Part 1, §4,5). [j] Use of local integrated column density and corresponding uncertainty (Part 1, §5). [k] Absolute accuracy of the full-foil mapping technique (Part 1, §4). [l] Error in energy calibration data. Correction minimal at the absorption edge (Part 1, §9). [m] Relative measurements and uncertainties after correcting for systematics. [n] Absolute measurements and uncertainties after normalizing to absolute thickness with full-foil map.

3. Comparison with theory

Figure 2 compares our measured mass attenuation coefficients with *FFAST* tabulated values (Chantler, 1995, 2000), *XCOM* tabulated values with Hartree–Slater non-relativistic wavefunctions including Scofield relativistic perturbations (Berger & Hubbell, 1987) (unrenomalized) and also renormalized values in a relativistic Hartree–Fock potential as defined by Scofield (1973). There is an agreement in experimental results with *FFAST* values in the range of 8.5 keV to the edge energy and above 12 keV. The deviation of calculated values from the *FFAST* values begins at around the edge energy (9.66 keV) and decreases and converges to a 1% discrepancy above 12 keV (see Fig. 1 of Part 1).

At lower energies the variation of our experimental measurements is smooth (Fig. 1). The deviation from the *XCOM* values also begins at the edge with 5–10% uncertainty or error. Above the absorption edge, the experimental values deviate up and down significantly due to the oscillatory XAFS as expected. There is a dramatic discrepancy of *XCOM* theory with the experimental measurement at the white line, likely due to the inaccuracy of the edge energy predicted by *XCOM*. Whilst the experimental claimed accuracy is much better than this, the theoretical claimed uncertainty far above the (*K*) edge is about 1%, as observed. Perhaps surprisingly, given other high-accuracy results, *XCOM* has a 2–5% discrepancy from experimental results below the edge, favouring *FFAST*; though the two theoretical predictions are in very good agreement with one another above about 10.3 keV. Both disagree with both high-accuracy experiments.

Scofield (1973) discussed and provided two theoretical predictions for atomic absorption coefficients – the unrenormalized values in *XCOM* and another *renormalized* set, obtained by renormalizing the cross sections by the amplitude of the potential at the nucleus, in a relativistic Hartree–Fock potential compared with *XCOM*'s Hartree–Slater potential.

The decision as to whether or not to perform this renormalization has been an ongoing discussion in the field. Some previous investigations have favoured the unrenormalized results (Saloman & Hubbell, 1987), whilst some have claimed that the difference in the estimates should be used as an uncertainty, and that the correct value should lie between the two approaches (Gerward, 1992).

Those comparisons were made with significantly less accurate experimental data than that presented in this work, making a definitive resolution to this discussion impossible at that time. At all energies, *XCOM* [using Hartree–Slater (HS) non-relativistic wavefunctions] is more consistent with experimental data than the renormalized data referencing Hartree–Fock (HF) calculations. At lower energies, the discrepancy from the current experimental results is about 3% for *XCOM* data with HS calculations whereas data with HF calculations have a (much) higher (12%) discrepancy below 9.6 keV. This current evidence justifies the less-fully relativistic unrenormalized HS results [*XCOM*] over the HF renormalized data. Note that *FFAST* is a better relativistic and self-consistent model and in turn appears in better agreement with the experimental data.

The experimentally calculated data deviate from the theory by about 10–20% at the edge, 2.5% after the edge and 1–2% far above and below the edge. About 70% of the experimentally calculated data are in agreement (within 1–2σ) with *FFAST*. The XAFS oscillations near the edge are absent in theory because the theory was developed as a free-atom model and so deviations are therefore large near the edge energy. More importantly, the near-edge region shows a generally triangular discrepancy quite separate from the oscillatory solid state effects. This is a general observation for many materials such as silver (Tran *et al.*, 2005; Islam *et al.*, 2014; Tantau *et al.*, 2015), molybdenum (de Jonge *et al.*, 2005; Chantler & Bourke, 2010), tin (de Jonge *et al.*, 2007), copper (Chantler *et al.*, 2001; Glover *et al.*, 2008) and gold (Glover *et al.*, 2010; Islam *et al.*, 2010). Improvements in theoretical understanding are definitely required in the future especially for the baseline.

Data from Rae *et al.* (2010) are compared with these results over the common energy range, as it has the highest previous claimed accuracy of 0.044% to 0.197%. Rae *et al.* (2010) performed an X-ray absorption spectroscopy (XAS) experiment for zinc material on a different beamline using a similar technique. However, these detailed approaches in analysis were quite different. At lower energies our current results and Rae *et al.* (2010) are in excellent agreement (1σ). Rae *et al.* (2010) provide no XAFS and the spacing is unsuitable for any detailed nanostructure determination. However, it ought to be useful for an absolute measurement of the attenuation. These experimental results are in fair agreement with the earlier high-accuracy results to about 0.1% or 1–3σ of the earlier high-accuracy data set. The signature for the deviation can be investigated from the original paper, and may be due to harmonic, roughness or bandwidth in either analysis. Blank and dark-current normalization were performed in both experiments and the pattern of discrepancy does not match

these possible sources of systematic error. The energy calibration could provide this signature noting that the absence of XAFS and near-edge structure prevents the confirmation of this systematic or the confirmation of its absence. Perhaps the most likely cause is a systematic error of the previous analysis of scattering which decreases from 3% to 6% just above the edge to 1–2% or 2–4% around 11.5 keV. The current work corrected for significant direct scattering but also for significant background scattering whereas the earlier work only investigated direct scattering (Ekanayake *et al.*, 2021).

Other existing experimental data of Unonius & Suortti (1989) and Hopkins (1959) were compared in Fig. 1 of Part 1. Due to the lack of correction for numerous systematics, it is not surprising that discrepancies from current experiment and theory are 10–13%. These measurements are also sparse and provide no XAFS to confirm energy analysis. High-accuracy measurements with absolute uncertainties can therefore be used in understanding theoretical tabulations and limiting atomic physics modelling and nanostructural models. The derived mass attenuation coefficients are useful in solid-state and atomic fields in investigating many-body effects such as core-hole lifetime, interatomic interactions, threshold energy and thermal effects.

4. X-ray absorption edge jumps and edge jump ratios

The mass attenuation coefficient is related to the total attenuation cross section σ_{tot} (barns atom^{-1}) by

$$\sigma_{tot} = \left[\frac{\mu}{\rho}\right]\frac{A}{N_A}, \qquad (3)$$

where N_A is the Avogadro number and A is the atomic weight. The difference between the mass photoabsorption coefficient above and below the edge gives the K-shell mass photoabsorption coefficient and then the jump ratio is

$$r_K = \frac{\tau_K + \tau_L + \tau_M + \ldots}{\tau_L + \tau_M + \ldots} = \frac{[\mu/\rho]_{pe,\,above\,edge}}{[\mu/\rho]_{pe,\,below\,edge}}, \qquad (4)$$

where $\tau_i = [\mu/\rho]_{pe,i}$ (cm^2 g^{-1}) is the photoelectric absorption coefficient for the shell i. The K-shell jump factor is then defined as (Latyshev, 1947; Schmickley & Pratt, 1967)

$$J_K = \frac{r_K - 1}{r_K} = \frac{\tau_K}{\tau_K + \tau_L + \tau_M + \ldots}$$
$$= \frac{[\mu/\rho]_{pe,\,above\,edge} - [\mu/\rho]_{pe,\,below\,edge}}{[\mu/\rho]_{pe,\,above\,edge}}. \qquad (5)$$

Four main methods for calculating the edge jump ratio and jump factor are reported:

(1) A gamma-ray attenuation method, where gamma-rays are attenuated through a sample and the attenuation coefficient is determined (Puttaswamy *et al.*, 1981; Ouseph *et al.*, 1982; Mallikarjuna *et al.*, 2002). The early key idea was to have a radioactive source with lines on either side of the absorption edge and use the relative attenuation to determine the jump ratio and jump factor for the edge. Uncertainties of order 5% are reported; however, in this approach, the energies of the

two lines are often significantly (very) far apart, *e.g.* 7 keV or 12 keV or 20 keV away from the edge; and hence interpretation of the edge jump is seriously limited by the extrapolation required.

(2) A Compton peak attenuation method, where the broad Compton-scattered spectral photons are allowed to attenuate through an elemental solid to measure attenuation coefficients above and below the edge for the continuum spectrum (Ayala & Mainardi, 1996; Budak & Polat, 2004; Polat *et al.*, 2004). Measurement step sizes are typically 50 eV or 58 eV. Uncertainties are estimated as 1.5%, although discrepancies of 5% are observed.

In methods (1) and (2), no influence of scattering or fluorescence on the measurement is normally corrected for. This introduces a somewhat ill-defined uncertainty and systematic error. In general, this is similar to replacing $[\mu/\rho]_{pe}$ with $[\mu/\rho]$, so that typically the numerator and denominator of equation (4) are increased by a scattering offset; and the denominator of equation (5) is increased by the same amount. In both methods (1) and (2), normally only one experimental sample thickness is measured. Although in an ideal situation this might yield a correct result, this manuscript and Part 1 prove that the thickness dependence of systematics is quite significant.

(3) An energy-dispersive X-ray fluorescence (EDXRF) method, where X-ray photons are allowed to pass through a sample and then the attenuation is measured (Ertugrul *et al.*, 2002; Budak *et al.*, 2003; Polat *et al.*, 2005; Bennal & Badiger, 2007; Kaya *et al.*, 2011; Singh Sidhu *et al.*, 2011). This method derives the jump factor using the fairly complex expression

$$J_K = \frac{\sigma_{K\alpha}}{(\sigma_{\mathrm{tot}} - \sigma_{\mathrm{ts}})\,\omega_K} \left(1 + \frac{I_{K\beta}}{I_{K\alpha}}\right). \tag{6}$$

Whilst this equation quotes the cross sections in barns atom^{-1}, this is exactly equivalent to using the mass attenuation coefficients in cm^2 g^{-1}. The method measures the intensity in fluorescence of the two characteristic radiations $I_{K\alpha}$, $I_{K\beta}$; and separately measures the mass attenuation coefficients. The method requires: that the self-absorption of the two characteristic radiations ($K\alpha$, $K\beta$) are computed in fluorescence using theoretical mass attenuation coefficients (Trevorah *et al.*, 2019); that the K-shell fluorescence yield ω_K is taken from an available tabulation (*e.g.* Broll, 1986; Bambynek *et al.*, 1972); that the efficiencies of the detector at the two characteristic energies are known; and that separately the scattering coefficients σ_{ts} are taken from a suitable tabulation (*e.g.* Berger & Hubbell, 1987; Chantler, 1995). Typical uncertainties are estimated as 3–8%, yet the uncertainties in the contributing theoretical corrections are significant. Scattering may or may not be corrected for in the extracted numerator and denominator.

A variation of this method produces secondary characteristic $K\alpha$, $K\beta$ spectra from a radioactive source incident on several targets. Spectra are then measured using an EDXRF spectrometer to measure the attenuation coefficient of the sample across the energy resolution of the detector with good statistics in the region of the characteristic radiation (Kaya *et*

al., 2007). Without correction for scattering, this will measure ratios based on attenuation coefficients rather than photoelectric coefficients. Kaya *et al.* (2011) comment that the absorption curves are often distorted above the edge leading to major challenges in defining a clear attenuation or absorption coefficient (XAFS); and similarly that scattering is quite significant at these energies and will generally lead to ratios of attenuation coefficient being measured instead of photoabsorption.

(4) A Bremsstrahlung transmission method, where a continuous bremsstrahlung radiation is allowed to pass through a sample to determine a sudden drop in intensity (Nayak & Badiger, 2006) across the edge, and then used for measuring the absorption jump ratio and factors. In principle, this is a direct attenuation measurement with potentially fine spacing (50–600 eV) around the edge, and by fitting the above-edge and below-edge region (neglecting XAFS) one can derive the relevant attenuation coefficients, from which the photoelectric absorption coefficients can be extracted.

We, however, measure the zinc K-edge jump, jump ratio and jump factor from the current data herein and hence use an alternative XERT-like method. Synchrotron X-rays are allowed to pass through the sample to measure attenuation coefficients, from which photoabsorption coefficients and edge-jump ratios can be derived (Chantler *et al.*, 2001; Rae *et al.*, 2010; Sier *et al.*, 2020). Following Fig. 3, we initially removed the pre-edge background. Then we investigated the structure of the oscillation, defined spline and removed the spline. Far above the edge, the theory and experiment presented here are in good agreement. A key issue is the challenge to extrapolate the curves from below and from above the edge to define or extract the edge jump and the relevant cross sections.

The 'triangle effect' implies that near the edge both *XCOM* and *FFAST* underestimate the average experimental
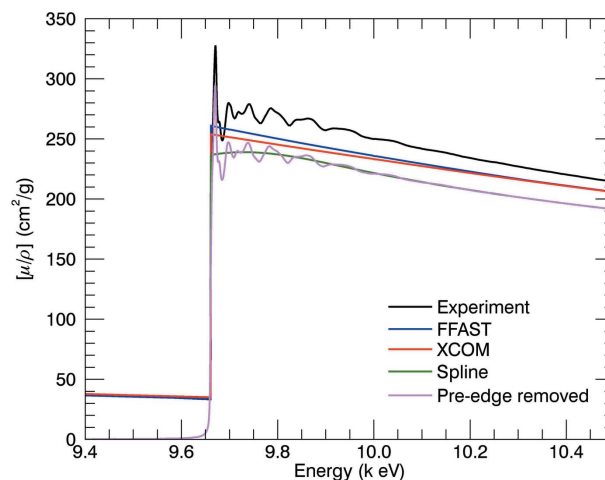
Figure 3
As with XAFS analysis, the slope of the pre-edge is extrapolated to the edge energy. The value of the spline through the above-edge data at the (above-)edge position is taken as the above-edge value. Therefore the XAS structure above the edge is fitted to a low-order piece-wise continuous polynomial.

Table 2
Derivation of above- and below-edge ratios based upon $[\mu/\rho]_{tot}$ or $[\mu/\rho]$ (see text).

Source	$[\mu/\rho]_{tot}$ $(E < E_K)$ 'B' (cm² g⁻¹)	$[\mu/\rho]_{tot}$ $(E > E_K)$ 'A' (cm² g⁻¹)	Jump 'A' − 'B' (cm² g⁻¹)	$r_{K,tot}$ 'A'/'B'	$J_{K,tot}$ ('A' − 'B')/'A'
XCOM[a]	35.098	253.951	218.853	7.236	0.862
FFAST[b]	33.810	260.906	227.096	7.717	0.8704
This work	33.369	269.991	236.622	8.091	0.8764
Estimate minimum σ	0.3	3.0	3.0	0.116	0.0148
Zn $Z = 30$[c]				7.602	0.868[d]
Zn[eg]				7.692	0.870
Zn[fg]				7.547	0.867
Zn[bg]				7.592	0.868
Zn[hg]				7.103	0.859
Zn[g]				7.633	0.869

[a] XCOM (Scofield, 1973; Berger & Hubbell, 1987). [b] FFAST (Chantler, 2000). [c] McMaster et al. (1969). [d] Broll (1986). [e] Storm & Israel (1970). [f] Gerward et al. (2001). [g] Singh Sidhu et al. (2011). [h] Rae et al. (2010).

Table 3
Experimental and theoretical values of the K-shell absorption jump factor and jump ratio for zinc metal.

Source	$[\mu/\rho]_{pe}$ $(E < E_K)$ 'B' (cm² g⁻¹)	$[\mu/\rho]_{pe}$ $(E > E_K)$ 'A' (cm² g⁻¹)	Jump 'A' − 'B' (cm² g⁻¹)	r_K 'A'/'B'	J_K ('A' − 'B')/'A'
XCOM[a]	33.413	252.267	218.853	7.5450	0.8675
FFAST[b]	32.068	259.164	227.096	8.082	0.8763
This work[c]	31.627	268.250	236.622	8.482	0.8821
Estimated σ	0.3	3	3	0.124	0.0149

[a] XCOM (Berger & Hubbell, 1987) using $[\mu/\rho]_{R+C}$ $(E = E_K) \simeq 1.684$ cm⁻² g⁻¹. [b] FFAST (Chantler, 2000) using $[\mu/\rho]_{R+C}$ $(E = E_K) \simeq 1.742$ cm⁻² g⁻¹. [c] Using $[\mu/\rho]_{R+C}$ $(E = E_K) \simeq 1.742$ cm⁻² g⁻¹ (Chantler, 2000).

attenuation coefficient. *FFAST* performs better than *XCOM*. However, both theoretical predictions continue to increase towards the edge from above the edge, roughly as $(E - E_K)^{-3}$; however, the imputed spline from experimental data passing through the XAFS and XANES structure curves downwards towards the edge. The correct theoretical prediction, or equivalently the correct form for the spline near the edge, is currently not yet known.

The theoretical predictions are well defined and have low uncertainty *per se*. However, there is likely a discrepancy separate from the complexity of the XAFS structure in matching the edge jump ratios and edge jump factors.

On the experimental side above the edge for many materials including ideal metals and elemental solids, the selection of one particular spline and form can easily change the above-edge estimate of the attenuation coefficient by about 3 cm² g⁻¹ in this case or by about 1% in general.

Below the edge the issue of extrapolating to the edge whilst avoiding any pre-edge structure or indeed the beginning of the edge is a challenge even if very fine point spacing is used, so we estimate an uncertainty from this of about 0.3 cm² g⁻¹ in this case or perhaps 1% in general. Therefore both the experimental and the theoretical uncertainty of $[\mu/\rho]_{tot}$ $(E < E_K)$, 'A', and $[\mu/\rho]_{tot}$ $(E > E_K)$, 'B', in Table 2 can be estimated by the difference between, for example, two estimates from different splines or different extrapolation methods, or different theoretical predictions. In Table 2 we have propagated the uncertainties assuming that the cause of a systematic

in 'A' or 'B' are uncorrelated. In expressions involving 'A'/'A', for example, the correlated uncertainty cancels. The statistical propagation of uncertainty neglecting this potential systematic (*i.e.* uncorrelated uncertainty) is a full factor of ten smaller (± 0.012 for r_K and ± 0.0015 for J_K).

We then compare the data directly from *XCOM* and *FFAST* with that from this work. Discrepancies are real and yet there is a good consensus. Comparing with the literature for Zn edge jump ratios and edge jump factors in the literature reveals some good consistency. However, even for the stable theory with no XAFS structure, reference *a* should be identical to reference *f* (see footnote of Table 2) and is at least an underestimate of the associated error in extrapolation for the theory. Above the edge, *XCOM* is anomalously low compared with experiment or *FFAST*; below the edge it is anomalously high; hence the edge jump ratio is anomalously low.

There is a particularly strong discrepancy for McMaster *et al.* (1969) (reference *c* in Table 2) between the adjacent elements which is not replicated in other theory or experiment, which could be due to a typographic or convergence error; or could be due to the issue of scattering. Data from McMaster *et al.* (1969) are taken from a variety of sources, and therefore inherently inconsistent. Given the definitions and equations above, we recompute these ratios in Table 3 after subtracting off elastic and inelastic scattering (Rayleigh and Compton scattering contributions to attenuation) so that we can report ratios of photoabsorption as defined. In this paper, we have used Chantler (2000) for scattering components, ideal for

amorphous systems or metals. In oriented crystals the coherent cross-section follows Bragg–Laue scattering or thermal diffuse scattering; these coefficients are very different from Chantler (2000) or Scofield, 1973) and Berger & Hubbell (1987). In any case, the edge jump ('A' − 'B') is independent of this scattering contribution as seen in the tables. Correction for scattering increases the values of J_K from the previous table by about 0.006; and similarly increases the values of r_K by about 0.39, much larger than claimed respective uncertainties. With the exception of the anomalous value for McMaster *et al.* (1969), none of the experimental or other theoretical values appear to follow the formulae stated using $[\mu/\rho]_{pe}$. Instead all of them appear to take ratios of *attenuation coefficients* $[\mu/\rho]_{tot}$. In light of this, we define (or redefine) the *attenuation edge jump ratio and factor* to be $r_{K,tot}$ and $J_{K,tot}$.

With these difficulties, one might question the utility of the edge jump ratios and edge jump factors. However, they remain extremely important if non-trivial to extract experimentally. The widespread use of XRF and EDXRF argues strongly for increased understanding of these ratios and how to use and interpret them; the propagation errors and uncertainties of XANES and XAFS analysis, especially at low k, depend upon the stability and uniqueness of the definition of the edge and spline or other background subtraction; and more theoretical and experimental work is required in this area in attenuation, absorption and fluorescence measurements. Immediately, we can use this analysis to justify the data presented herein; and to emphasize or demonstrate the error of Singh Sidhu *et al.* (2011) observed in Table 2 [references Singh Sidhu *et al.* (2011) and Rae *et al.* (2010)].

Previous work to obtain the edge jumps of the zinc K-edge using this method (Sier *et al.*, 2020) on zinc selenide found the jump ratio to be $r_{K,tot}$ = 3.380. However, as this work was conducted on a compound, this value must be scaled by the relative atomic composition of zinc within zinc selenide (0.453) which converts the value to $r_{K,tot}$ = 7.461 as the attenuation ratio; and to r_K = 3.406 as the photoabsorption ratio in the compound, and r_K = 7.519 as the photoabsorption ratio for the Zn. Note that ZnSe does not have Rayleigh scattering but rather thermal diffuse scattering, so the elastic scattering coefficients are necessarily different from the tabulations. Similarly, in that work $r_{K,tot}$ = 2.153 was reported for the Se K-edge jump ratio with r_K = 2.161 for the compound, and $r_{K,tot}$ = 3.936 and r_K = 3.951 for the selenium edge.

Rae *et al.* (2010) measured the attenuation coefficient of pure zinc metal. The data are far too sparse to enable effective spline fitting of the XAFS above the edge; or to extract a good below-edge background. Taking a ratio of the photoabsorption data points closest to the edge results in an r_K of 7.426. The sparse nature of this data means that the post-edge point is significantly lower in attenuation than the true pre-edge, thus leading to a lower r_K.

Overall for Zn metal we are able to report *absorption ratios* r_K = 8.482 (12) (124) where the first uncertainty is statistical and the second is systematic; and J_K = 0.882 (15) (149); and we are able to report $r_{K,tot}$ = 8.091 (12) (116); and $J_{K,tot}$ =

0.8764 (15) (148) following past evaluations using the *attenuation coefficient ratios*. These measurements are and must be higher than the theoretical predictions of either *FFAST* or *XCOM*, though *FFAST* is almost within uncertainty of the experiment, which is promising for future work. This confirmation allows us to proceed with some confidence to investigating the nanostructure from the XAFS signal.

5. X-ray absorption fine structure

The XAFS of zinc above the zinc K-edge (Fig. 1) probes the oscillations of the photoabsorption coefficients above the edge due to the photoelectron interference. The oscillatory part of the spectrum was isolated using the fine-structure function

$$\chi(E) = \frac{\mu(E) - \mu_0(E)}{\mu(E_0)}, \qquad (7)$$

where $\mu_0(E)$ is a smooth atom-like background, E_0 is the edge energy – ideally the onset of the open channel to the continuum but often (as here) estimated by the maximum of the first derivative across the edge. χ is then expressed as a function of k, the effective photoelectron wavenumber,

$$k = \left[\frac{2m_e}{\hbar^2}(E - E_0)\right]^{1/2}, \qquad (8)$$

where m_e is the mass of an electron, E is the photon energy and E_0 is the edge energy.

The background function $\mu_0(E)$ is obtained from an approximated spline using the *eFEFFIT* package (Smale *et al.*, 2006; Schalken & Chantler, 2018). The spline approach has been widely used to isolate the oscillatory part in the XAFS community for several decades (Newville *et al.*, 1993; Smale *et al.*, 2006; Islam *et al.*, 2016). The uncertainty of the oscillatory measurements was quantified using

$$\sigma_{\chi(k)} = \frac{\sigma_{\mu(E)}}{\mu(E_0)}, \qquad (9)$$

where $\sigma_{\chi(k)}$ is the uncertainty of $\chi(k)$ and $\sigma_{\mu(E)}$ is the experimental uncertainties of the X-ray absorption measurements. Figure 4 illustrates the oscillatory part of the XAFS spectrum with fully propagated uncertainties.

The XAFS equation describes the oscillatory part $\chi(k)$ as a sum over the multiple scattering paths,

$$\chi(k) = \sum_j N_j S_0^2 F_j(k) \frac{\sin[2kr_j + \phi_j(k)]}{kr_j^2}$$
$$\times \exp(-2\sigma_j^2 k^2) \exp[p - 2r_j / \lambda(k)], \qquad (10)$$

where j denotes the jth path, N_j is the degeneracy, S_0^2 is the many-body reduction factor, $F_j(k)$ is the backscattering amplitude function, r_j is half the path length, $\phi_j(k)$ is the total phase shift function, σ_j is the Debye–Waller factor and $\lambda(k)$ is the photoelectron mean free path function. A dominant standard approach for XAFS analysis uses equation (10), perhaps particularly via the *IFEFFIT* computational package (Newville, 2001) together with *FEFF* (Rehr & Albers, 2000;
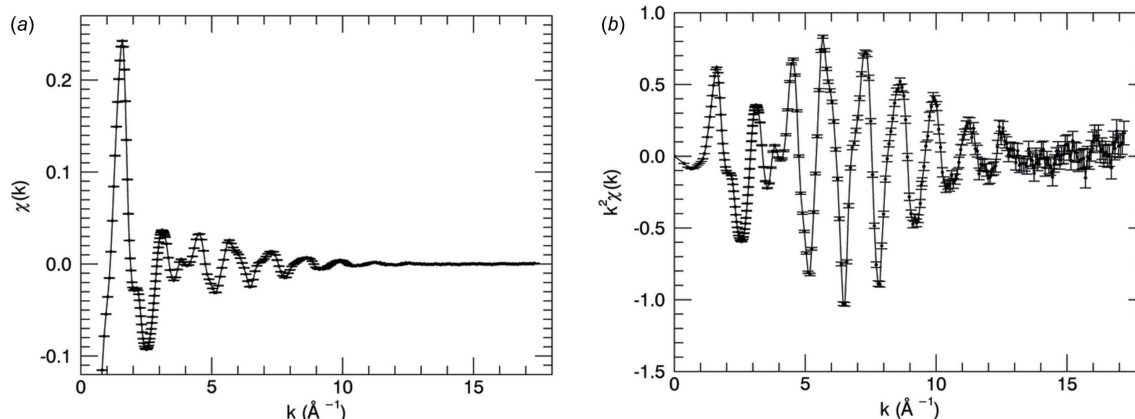
Figure 4
The fine-structure function of the zinc K-edge produced by the *Mu2chi* non-interpolation background subtraction software in the *eFEFFIT* package.

Rehr *et al.*, 1991), to investigate the local nanostructure of materials. The lattice constants of zinc have been determined by single-crystal X-ray diffraction, to be a = 266.36 (1) pm and c = 494.57 (2) pm with c/a = 1.857 at a temperature of 300 K (Hull & Davey, 1921; Nuss *et al.*, 2010). Zinc is located at the special Wyckoff position $2c$ $(1/3, 2/3, 1/4)$ in space group $P6_3/mmc(194)$. The theoretical prediction from *FEFF* was used in *eFEFFIT* (Smale *et al.*, 2006; Schalken & Chantler, 2018), modified from the *IFEFFIT* package to propagate uncertainties. Data were fitted across several k-ranges to investigate robustness. Most effective was the range of k from 4.5 Å^{-1} to 17 Å^{-1} using absolute uncertainties of input data. Below this range, the theory underpinning the fitting function begins to break down. Above this range the uncertainties prove that the data are now dominated by noise.

After extensive analysis, the two nearest-neighbour bond lengths, also with the highest ranks from *FEFF*, were given two separate fitting parameters, whilst all other bond lengths were scaled by the usual α (Ravel, 2005). Independent σ_i^2 were used for the two nearest-neighbour bond lengths (Ravel & Kelly, 2007; Kelly *et al.*, 2002; Ravel, 2009). Linear paths were quantified in terms of the σ_i^2 values of the single-scattering paths that contain the end atoms (Hudson *et al.*, 1995). Particular paths for double forward-scattering followed recommendations from Ravel (2016) about increased thermal parameters expected ($2\sigma_i^2$ and $1.5\sigma_i^2$ depending upon path combination). *FEFF6* and *FEFF8* gave similar results, parameters, uncertainties and χ_r^2. Path information and ordering does change between the versions, so parameter files need to be checked carefully in going from one to the other. Results presented here are for *FEFF6*.

This analysis expanded the scattering to 45 paths, *i.e.* out to a maximum $R \simeq 6.7$ Å. A model with a single scale α and a single thermal parameter σ^2 fails with χ_r^2 = 290, and a model with an α and σ^2 assigned to the nearest-neighbour bond length and another α and σ^2 to all other paths also fails with χ_r^2 = 16.8. Increasing the number of σ^2 parameters to three is necessary and significant and a model with a single scale α yielded χ_r^2 = 18.1, and a model with an α assigned to the nearest-neighbour bond length and another to all other paths

yielded a relatively poor χ_r^2 = 14.4. A developed model with three α and three σ^2 values for the relevant paths led to χ_r^2 = 9.5. Finally, incorporating a σ_4^4 value for two single-scattering paths ('8' and '9') led to the final χ_r^2 = 6.66. Other investigations of further independent parameters including a separated α showed insignificant improvement of the fits. However, note that the space is highly correlated in this area.

The incorporation of the path lengths and σ^2 parameters led to uncertainties in these parameters reducing from 0.5% to between 0.10% to 0.29% for the bond lengths or to ± 0.003 Å to ± 0.008 Å; and led to σ^2 thermal parameters with uncertainties around 3–5%. Perhaps more significantly, S_0^2 converged from the simpler fits with fewer parameters of 1.7 ± 0.3 to 0.904 ± 0.037 with four independent σ_i^2 parameters.

This demonstrates the need for four independent σ^2 thermal parameters, and the need for three independent path length scalings. Whilst the parameters are moderately robust in these simpler analyses, the fits are poor *until* the two shortest bond lengths are given independent path lengths and thermal broadening.

Zinc could have a single scaling (expansion) parameter relative to a crystallographic determination, if the metal is ideal at zero temperature; or of course if the crystallographic structure, the difference between mean lattice sites, were fully consistent with the dynamical bond lengths and path lengths. In this experiment, however, dynamical motion at room temperature might be expected to lead to significant variation of expansion of the path lengths relative to a corresponding crystallographic determination. Fitted parameters are summarized in Table 4 and results are illustrated in Fig. 5. Fits give good physical agreement and parameters are consistent within 1σ.

An interesting result of this analysis is the different expansions obtained for the nearest and second-nearest scattering paths. The reported nearest-neighbour and the second-nearest-neighbour Zn—Zn bond lengths are 2.6636 Å and 2.9120 Å (Nuss *et al.*, 2010) (Fig. 6). This work determines bond lengths 0.11% (± 0.10%) and 2.7% (± 0.3%) *smaller*, respectively. The scaling parameter obtained for the other

Table 4
FEFF6 and *eFEFFIT* parameters.

Parameter	Value	Error
S_0^2	0.904	0.037
E_{corr}^0	4.70 eV	0.29 eV
Zn—Zn ^{a}	2.660 Å	0.003 Å
Zn—Zn ^{b}	2.832 Å	0.008 Å
$\alpha_1{}^a$	0.9999	0.0010
$\alpha_2{}^b$	0.9737	0.0027
$\alpha_3{}^c$	1.0061	0.0013
$\sigma_1^{2\,a}$	0.0101 Å^2	0.0003 Å^2
$\sigma_2^{2\,b}$	0.0198 Å^2	0.0008 Å^2
$\sigma_3^{2\,c}$	0.0221 Å^2	0.0007 Å^2
$\sigma_4^{2\,d}$	0.0169 Å^2	0.0008 Å^2
χ_r^2	6.66	

^{a} For nearest-neighbour (shortest) scattering path. ^{b} For the second nearest atom. ^{c} Most other scattering paths (see supporting information for a full listing). ^{d} For single-scattering paths '8' and '9'.
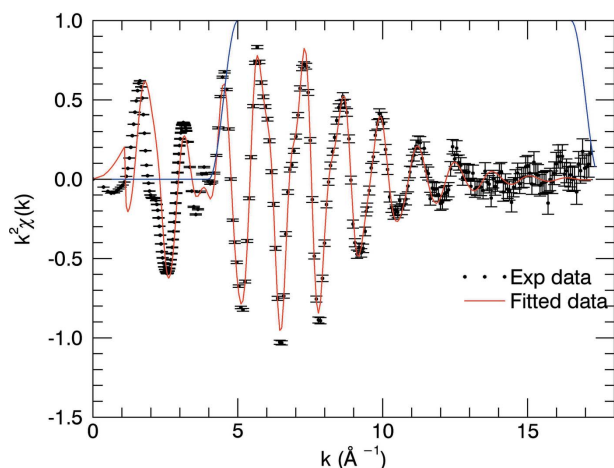

Figure 6
Crystal structure of zinc at 300 K with a form of hexagonal close packing, in which each atom has six nearest neighbours at 2.66 Å in its own plane and others at a greater distance of 4.95 Å.

Figure 5
Experimental data (black) with absolute uncertainties and the fitted model (red) across $k = 4.5$ Å^{-1} to 17 Å^{-1} for the zinc K-edge. Data were fitted over a Hanning window.

bond lengths are 0.62% ± 0.13% *larger* than the scaling of the nearest neighbour bond length.

These 5–7 standard error variations can be due to dynamic motion, or to the path-length including motion perpendicular to the bond length. XAFS is sensitive to atomic vibrations perpendicular to the bond direction, and to (positively or negatively) correlated motion of the atoms of the corresponding bond to increase or decrease the bond length compared with the crystallographic lattice site separation. Hence a bond length 0.004 Å to 0.08 Å smaller than X-ray diffraction (XRD) results at room temperature would be no surprise especially if the motion of both atoms was positively correlated.

The shift of next-neighbour bond lengths compared with XRD may alternatively be due to the sensitivity with temperature to the c/a axis. According to crystallographic determinations, a 5 K error in temperature would have only a shift of c/a of order 0.0003 Å so is inadequate to explain the lattice variation observations. Similarly, rolled foils have some static disorder from twinning or stacking faults, compared for example with an ideal crystal structure. Changing *ABABAB*
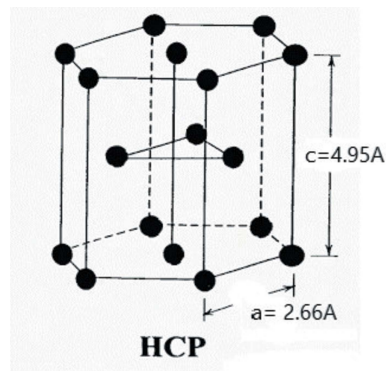
to *ABABCAB* compromises the assigned Wykoff positions in the earlier calculations. This static disorder would then confuse the separation of static disorder from thermal disorder. This question can explicitly be clarified with a temperature series. To first order this will increase the disorder, *i.e.* the σ on the bond lengths, rather than the bond lengths themselves. In particular, this will increase the σ or mean isotropic thermal parameters for farther atomic pairs. To second order this would increase the bond lengths or lattice separations especially with a high density of phase boundaries, stacking faults or microstructure such as twinning. However, the largest observed effect with respect to the nearest-neighbour bond length is a decrease rather than an increase, so is the incorrect sign. The bond lengths fitted for the farther Zn moieties is an increase so may be augmented by such details. In fact, we know that thermal parameters increase with path length and distance, and this is naturally due to the increasing disorder, static and dynamic, as seen in most XAS studies. The uncertainty of the larger bond lengths is about 0.13% suggesting significant variation of bond lengths, and supported by the increased thermal parameters.

In this case the evidence is inconclusive, but quite suggestive of local dynamical motion and local order combined with distant increasing static disorder. Hence this suggests dynamic motion in the crystal lattice inaccessible to other techniques.

6. Conclusion

X-ray mass attenuation coefficients and the imaginary component of the atomic form factor of zinc were measured over the energy range from 8.51 keV to 11.5914 keV including the zinc K-edge and XAFS with 496 data points at different energies. The accuracy of measured mass attenuation coefficients is about 0.023% to 0.036% and some 50% better than previous claims. These measurements are the most accurate zinc K-edge data set.

Comparison of the experimental data with the tabulated *FFAST* and *XCOM* theory shows very good agreement. The edge jump and jump ratio analysis shows some discrepancies due to the challenges of defining both the below-edge and above-edge absorption coefficient, so that most of the

preceding literature uses ratios and jump factors for the attenuation coefficient thereby including scattering – we separate these ideas by defining (or redefining) the *attenuation* ratio and factor to be $r_{K,\text{tot}}$ and $J_{K,\text{tot}}$. These measures are also challenging because of the experimental pre-edge and edge-width below the edge; and of the typical use of splines to attempt to deal with the above-edge XAFS. Nonetheless, this is a valuable confirmation of the scaling and absolute value of the coefficients and can be used for any experiment as a test of the quality of the data and data processing.

The high-accuracy measurements were improved for structural investigations. Robust investigation of zinc nano-structure was carried out using *eFEFFIT* with propagated uncertainties from XERT. X-ray absorption fine-structure analysis shows an excellent agreement between the measured and tabulated values and yields bond lengths and nano-structure of zinc with uncertainties of 0.11% to 0.27% or 0.003 Å to 0.009 Å, respectively. Thermal σ^2 parameters were fitted with an accuracy of from approximately 5%, and S_0^2 is determined to be 0.904 ± 0.037. Observed significant variation from reported crystal structures suggests local dynamic motion compared with a standard crystal lattice and increasing static disorder as expected in a non-ideally crystalline environment such as a metal foil. XAFS is sensitive to dynamic correlated motion so is in principle able to observe local dynamic motion beyond the reach of conventional crystallography.

These high-accuracy studies also allow one to investigate solid state effects including inelastic mean free paths, and inelastic and elastic scattering cross-sections.

Acknowledgements

References

Ayala, A. P. & Mainardi, R. T. (1996). *Radiat. Phys. Chem.* **47**, 177–181.

Bambynek, W., Crasemann, B., Fink, R. W., Freund, H. U., Mark, H., Swift, C. D., Price, R. E. & Rao, P. V. (1972). *Rev. Mod. Phys.* **44**, 716–813.

Bennal, A. S. & Badiger, N. M. (2007). *J. Phys. B At. Mol. Opt. Phys.* **40**, 2189–2199.

Berger, M. J. & Hubbell, J. H. (1987). *XCOM: Photon Cross Sections on A National Bureau of Standards*. Technical Report NBSIR-87–3597. Center for Radiation, National Bureau of Standards, Washington, DC, USA.

Bohic, S., Simionovici, A., Snigirev, A., Ortega, R. G., Devès, D., Heymann, D. & Schroer, C. G. (2001). *Appl. Phys. Lett.* **78**, 3544–3546.

Broll, N. (1986). *X-ray Spectrom.* **15**, 271–285.

Budak, G., Karabulut, A. & Ertuğrul, M. (2003). *Radiat. Meas.* **37**, 103–107.

Budak, G. & Polat, R. (2004). *J. Quant. Spectrosc. Radiat. Transfer*, **88**, 525–532.

Chantler, C. T. (1995). *J. Phys. Chem. Ref. Data*, **24**, 71–643.

Chantler, C. T. (2000). *J. Phys. Chem. Ref. Data*, **29**, 597–1056.

Chantler, C. T. (2009). *Eur. Phys. J. Spec. Top.* **169**, 147–153.

Chantler, C. T. & Bourke, J. D. (2010). *J. Phys. Chem. Lett.* **1**, 2422–2427.

Chantler, C. T., Tran, C. Q., Barnea, Z., Paterson, D., Cookson, D. J. & Balaic, D. X. (2001). *Phys. Rev. A*, **64**, 062506.

Coulthard, I. & Sham, T. K. (1996). *Phys. Rev. Lett.* **77**, 4824–4827.

Ekanayake, R. S. K., Chantler, C. T., Sier, D., Schalken, M. J., Illig, A. J., de Jonge, M. D., Johannesen, B., Kappen, P. & Tran, C. Q. (2021). *J. Synchrotron Rad.* **28**, 1476–1491.

Ertugrul, M., Karabulut, A. & Budak, G. (2002). *Radiat. Phys. Chem.* **64**, 1–3.

Gerward, L. (1992). *Nucl. Instrum. Methods Phys. Res. B*, **69**, 407–412.

Gerward, L., Guilbert, N., Bjørn Jensen, K. & Levring, H. (2001). *Radiat. Phys. Chem.* **60**, 23–24.

Glover, J. L., Chantler, C. T., Barnea, Z., Rae, N. A. & Tran, C. Q. (2010). *J. Phys. B At. Mol. Opt. Phys.* **43**, 085001.

Glover, J. L., Chantler, C. T., Barnea, Z., Rae, N. A., Tran, C. Q., Creagh, D. C., Paterson, D. & Dhal, B. B. (2008). *Phys. Rev. A*, **78**, 052902.

Glover, J. L., Chantler, C. T. & de Jonge, M. D. (2009). *Phys. Lett. A*, **373**, 1177–1180.

Han, S., Stern, E., Haskel, D. & Moodenbaugh, A. R. (2002). *Phys. Rev. B*, **66**, 094101.

Hopersky, A., Petrov, I., Nadolinsky, A., Yavna, V. & Koneev, R. (2004). *J. Phys. B At. Mol. Opt. Phys.* **37**, 3313–3319.

Hopkins, J. I. (1959). *J. Appl. Phys.* **30**, 185–187.

Hossain, F. M., Riley, D. P. & Murch, G. E. (2005). *Phys. Rev. B*, **72**, 235101.

Hudson, E. A., Rehr, J. J. & Bucher, J. J. (1995). *Phys. Rev. B*, **52**, 13815–13826.

Hull, A. W. & Davey, W. P. (1921). *Phys. Rev.* **17**, 549–570.

Ignatov, A. Y., Ali, N. & Khalid, S. (2001). *Phys. Rev. B*, **64**, 014413.

Islam, M. T., Best, S. P., Bourke, J. D., Tantau, L. J., Tran, C. Q., Wang, F. & Chantler, C. T. (2016). *J. Phys. Chem. C*, **120**, 9399–9418.

Islam, M. T., Chantler, C. T., Cheah, M. H., Tantau, L. J., Tran, C. Q. & Best, S. P. (2015). *J. Synchrotron Rad.* **22**, 1475–1491.

Islam, M. T., Rae, N. A., Glover, J. L., Barnea, Z., de Jonge, M. D., Tran, C. Q., Wang, J. & Chantler, C. T. (2010). *Phys. Rev. A*, **81**, 022903.

Islam, M. T., Tantau, L. J., Rae, N. A., Barnea, Z., Tran, C. Q. & Chantler, C. T. (2014). *J. Synchrotron Rad.* **21**, 413–423.

Joly, Y. (2001). *Phys. Rev. B*, **63**, 125120–125130.

Joly, Y., Cabaret, D., Renevier, H. & Natoli, C. R. (1999). *Phys. Rev. Lett.* **82**, 2398–2401.

Jonge, M. D. de, Tran, C. Q., Chantler, C. T., Barnea, Z., Dhal, B. B., Cookson, D. J., Lee, W. & Mashayekhi, A. (2005). *Phys. Rev. A*, **71**, 032702.

Jonge, M. D. de, Tran, C. Q., Chantler, C. T., Barnea, Z., Dhal, B. B., Paterson, D., Kanter, E. P., Southworth, S. H., Young, L., Beno, M. A., Linton, J. A. & Jennings, G. (2007). *Phys. Rev. A*, **75**, 032702.

Kaya, N., Apaydin, G. & Tirasoglu, E. (2011). *Radiat. Phys. Chem.* **80**, 677–681.

Kaya, N., Tıraşoğlu, E., Apaydın, G., Aylıkcı, V. & Cengiz, E. (2007). *Nucl. Instrum. Methods Phys. Res. B*, **262**, 16–23.

Kelly, S. D., Kemner, K. M., Fein, J. B., Fowle, D. A., Boyanov, M. I., Bunker, B. A. & Yee, N. (2002). *Geochim. Cosmochim. Acta*, **66**, 3855–3871.

Latyshev, G. D. (1947). *Rev. Mod. Phys.* **19**, 132–145.

Mallikarjuna, M. L., Appaji Gowda, S. B., Gowda, R. & Umesh, T. K. (2002). *Radiat. Phys. Chem.* **65**, 217–223.

McMaster, W. H., Del Grande, N. K., Mallett, J. H. & Hubbell, J. H. (1969). *Compilation of X-ray Cross Sections.* Technical Report UCRL-50174. Lawrence Livermore Laboratory, USA.

Nayak, S. V. & Badiger, N. M. (2006). *J. Phys. B At. Mol. Opt. Phys.* **39**, 2893–2900.

Newville, M. (2001). *J. Synchrotron Rad.* **8**, 96–100.

Newville, M., Līviņ\us, P., Yacoby, Y., Rehr, J. J. & Stern, E. A. (1993). *Jpn. J. Appl. Phys.* **32**, 125–127.

Nuss, J., Wedig, U., Kirfel, A. & Jansen, M. (2010). *Z. Anorg. Allg. Chem.* **636**, 309–313.

Ouseph, P. J., Hoskins, K. D., Berman, J. I. & Bolander, A. J. (1982). *Am. J. Phys.* **50**, 275–276.

Palmberg, P. W. & Rhodin, T. N. (1968). *J. Appl. Phys.* **39**, 2425–2432.

Polat, R., Budak, G., Gürol, A., Karabulut, A. & Ertuğrul, M. (2005). *Radiat. Meas.* **39**, 409–415.

Polat, R., İçelli, O. & Budak, G. (2004). *Anal. Chim. Acta*, **505**, 307–314.

Puttaswamy, K. S., Gowda, R. & Sanjeevaiah, B. (1981). *Can. J. Phys.* **59**, 853–858.

Rae, N. A., Chantler, C. T., Barnea, Z., de Jonge, M. D., Tran, C. Q. & Hester, J. R. (2010). *Phys. Rev. A*, **81**, 022904.

Ravel, B. (2005). *J. Alloys Compd.* **401**, 118–126.

Ravel, B. (2009). *J. Phys. Conf. Ser.* **190**, 012026.

Ravel, B. (2016). *Artemis manual*, https://bruceravel.github.io/demeter/documents/Artemis/forward.html.

Ravel, B. & Kelly, S. D. (2007). *AIP Conf. Proc.* **882**, 150–152.

Ravel, B. & Newville, M. (2005). *J. Synchrotron Rad.* **12**, 537–541.

Rehr, J. J. & Albers, R. C. (2000). *Rev. Mod. Phys.* **72**, 621–654.

Rehr, J. J., Mustre de Leon, J., Zabinsky, S. I. & Albers, R. C. (1991). *J. Am. Chem. Soc.* **113**, 5135–5140.

Rontgen, W. (1896). *Nature*, **53**, 274–276.

Saloman, E. & Hubbell, J. (1987). *Nucl. Instrum. Methods Phys. Res. A*, **255**, 38–42.

Sayers, D. E., Lytle, F. W. & Stern, E. A. (1972). *J. Non-Cryst. Solids*, **8–10**, 401–407.

Schalken, M. J. & Chantler, C. T. (2018). *J. Synchrotron Rad.* **25**, 920–934.

Schmickley, R. D. & Pratt, R. H. (1967). *Phys. Rev.* **164**, 104–116.

Scofield, J. H. (1973). Technical Report UCRL-51326. Lawrence Livermore Laboratory, USA.

Sier, D., Cousland, G. P., Trevorah, R. M., Ekanayake, R. S. K., Tran, C. Q., Hester, J. R. & Chantler, C. T. (2020). *J. Synchrotron Rad.* **27**, 1262–1277.

Singh Sidhu, B., Dhaliwal, A. S., Mann, K. S. & Kahlon, K. S. (2011). *Radiat. Phys. Chem.* **80**, 28–32.

Smale, L. F., Chantler, C. T., de Jonge, M. D., Barnea, Z. & Tran, C. Q. (2006). *Radiat. Phys. Chem.* **75**, 1559–1563.

Storm, E. & Israel, I. H. (1970). *At. Data Nucl. Data Tables*, **7**, 565–681.

Streltsov, V. A., Ekanayake, R. S., Drew, S. C., Chantler, C. T. & Best, S. P. (2018). *Inorg. Chem.* **57**, 11422–11435.

Tantau, L. J., Chantler, C. T., Bourke, J. D., Islam, M. T., Payne, A. T., Rae, N. A. & Tran, C. Q. (2015). *J. Phys. Condens. Matter*, **27**, 266301.

Tran, C. Q., Chantler, C. T., Barnea, Z., Jonge, M. D., Dhal, B. B., Chung, C. T., Paterson, D. & Wang, J. (2005). *J. Phys. B At. Mol. Opt. Phys.* **38**, 89–107.

Trevorah, R. M., Chantler, C. T. & Schalken, M. J. (2019). *IUCrJ*, **6**, 586–602.

Unonius, L. & Suortti, P. (1989). *J. Appl. Cryst.* **22**, 46–52.

Veigele, W. J. (1973). *At. Data Nucl. Data Tables*, **5**, 51–111.